Advanced Infrared Thermography Data Analysis for Unsteady Boundary Layer Transition Detection

Mertens, Christoph; Wolf, C. Christian; Gardner, Anthony D.; Schrijer, Ferdinand; van Oudheusden, Bas

DOI
10.1088/1361-6501/ab3ae2

Publication date
2020

Document Version
Final published version

Published in
Measurement Science and Technology

PAPER

Advanced infrared thermography data analysis for unsteady boundary layer transition detection

IOP Publishing
Measurement Science and Technology
Meas. Sci. Technol. **31** (2020) 015301 (13pp)
https://doi.org/10.1088/1361-6501/ab3ae2

Advanced infrared thermography data analysis for unsteady boundary layer transition detection

C Mertens[1,2], C C Wolf[1], A D Gardner[1], F F J Schrijer[2] and B W van Oudheusden[2]

[1] Institute of Aerodynamics and Flow Technology, German Aerospace Center (DLR), 37073 Göttingen, Germany
[2] Faculty of Aerospace Engineering, Delft University of Technology, 2629 HS Delft, The Netherlands

E-mail: C.Mertens@tudelft.nl

Received 3 May 2019, revised 30 July 2019
Accepted for publication 13 August 2019
Published 16 October 2019

Abstract

Advanced data processing methods for detecting unsteady boundary layer transition in periodic aerodynamic processes by means of infrared thermography measurements are presented. The thermal radiation emitted from the heated suction surface of a pitching airfoil model in subsonic flow is measured with an infrared camera. The unsteady boundary layer transition location is detected by analyzing the difference in the infrared radiation signal over short periods of time with differential infrared thermography (DIT). The DIT method is optimized and automated in the present study, which facilitates the extension of the part of the motion period where valid DIT transition measurements are produced. Additionally, a new infrared thermography data processing method is introduced in this study. The extraction of the extrema of the measured radiation signal at fixed locations on the model surface yields instants of the motion period that relate to the occurrence of boundary layer transition. The local infrared thermography (LIT) approach can be extended to measuring the two-dimensional unsteady boundary layer transition front.

Keywords: unsteady aerodynamics, boundary layer transition, wind tunnel testing, pitching airfoil model, infrared thermography, data analysis

(Some figures may appear in colour only in the online journal)

1. Introduction

The laminar-turbulent boundary layer transition location is a crucial design parameter for airfoil aerodynamics. In aerodynamic problems with a cyclic variation of the inflow conditions, for example on helicopter rotors or wind turbine blades, the boundary layer transition location is unsteady. Current research studies on predicting the unsteady boundary layer transition location in this type of problem with computational fluid dynamics (CFD) rely on mathematical models including empirical factors [1]. Thus accurate experimental measurements of unsteady boundary layer transition for calibration and validation purposes are required.

From the wide range of available boundary layer transition measurement techniques such as oil flow interferometry [2], shear-stress sensitive crystals [3] or temperature-sensitive paint [4], traditionally only fast-response techniques can be applied in unsteady problems, in particular hot-film anemometry [5, 6]. While this long-established technique can provide detailed insights into the unsteady boundary layer flow [7], it is rather complex to implement, even when the data analysis is largely automated [8].

An alternative unsteady boundary layer transition measurement technique based on the analysis of fast-response surface pressure sensor signals has recently been developed by Gardner and Richter [9]. The σC_p-technique identifies the

occurrence of unsteady boundary layer transition on a pitching airfoil model as peaks in the standard deviation of the phase-averaged surface pressure coefficient measured over multiple pitching motion cycles. With the surface pressure sensors being an inherent part of many wind tunnel models, the experimental effort is reduced with the σC_p-technique [10].

Another approach to detecting unsteady boundary layer transition is infrared thermography (IRT). The first results for aerodynamics research with IRT were produced in a hypersonic wind tunnel as early as 1967 [11]. In the following years, advanced infrared camera technology played an important role in the space exploration efforts in the 1970s [12, 13]; later the main focus of aerodynamics research with IRT was shifted from hypersonic flows towards aerodynamics efficiency research, in particular boundary layer diagnostics in subsonic flows [14]. Today, IRT is an established experimental technique in aerodynamics, while the accuracy, spatial resolution and range of applications of IRT is ever increasing [15, 16].

The advantage of using IRT for unsteady boundary layer transition detection is that the optical measurement technique provides an increased spatial resolution of the measurements with a decreased experimental effort compared to the installed-sensor techniques, such as hot-film anemometry and σC_p. On the downside, the physical response time of the measured quantity, the model surface temperature, is larger than or at least at the same order of magnitude as the time scale of the aerodynamic unsteadiness. This results in continuously changing surface temperatures during the unsteady aerodynamics experiment, which impairs the conventional IRT data analysis method for detecting boundary layer transition and motivates the development of more advanced measurement data analysis methods.

The present study discusses advanced IRT data processing methods for unsteady boundary layer transition detection. The experimental data and simulation results in this study have been produced for previous studies at DLR Göttingen [17, 18] which were conducted to analyze and optimize the differential infrared thermography (DIT) method. This study provides a detailed analysis of the effect of the DIT image separation time step, summarizing the findings of previous studies. Based on this investigation, the DIT data analysis method is automated and extended in this study. Afterwards, a new approach for analyzing the IRT data is introduced, which provides a more detailed insight into the unsteady behavior of the boundary layer transition front on the model surface. A comparison of the unsteady transition measurement results from the advanced IRT data processing methods presented in this study is provided.

2. Infrared thermography for unsteady boundary layer transition detection

In steady subsonic aerodynamics, the boundary layer transition location can be determined from the IRT measurements [19] using the physical relation between the boundary layer state [20] and the convective heat transfer level [21], when

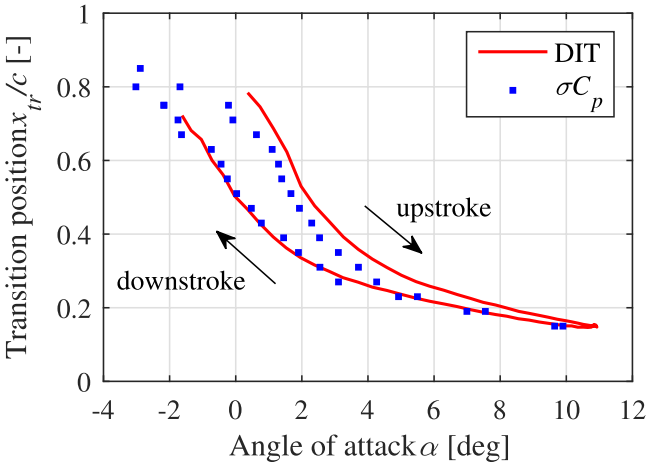

Figure 1. Optimized DIT result from Wolf *et al* [18].

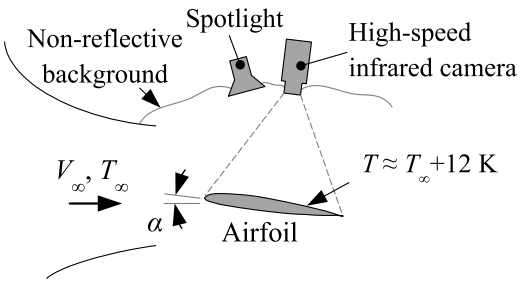

Figure 2. Experimental setup sketch, adapted from [18].

a temperature difference between the flow and the surface under investigation is established and a thermal equilibrium is reached. The same physical relations hold in unsteady aerodynamic problems, but when considering common aerospace materials (e.g. carbon or glass fiber-reinforced polymers) at technically relevant frequencies (around 6 Hz for helicopters), the time scale of the surface temperature response is larger than the period of the aerodynamic unsteadiness and no thermal equilibrium is reached on the surface. When the surface temperature is continuously changing, a single thermographic measurement cannot be used to determine the unsteady boundary layer transition position because it does not necessarily reflect the current position. The thermal response time of the surface can be improved by changing the heating mode or the surface material properties [22], but these modifications can be difficult to implement and they do not eliminate the general problem. Therefore, recent research on unsteady boundary layer transition has focused on the development of novel processing methods for IRT data measured in unsteady aerodynamics experiments.

In 2014, Raffel and Merz [23] proposed an unsteady transition detection method called differential infrared thermography (DIT) that is based on the subtraction of subsequent thermographic measurements. The principle of DIT is measuring the moving boundary layer transition as the maximum absolute difference between the measurements over a particular time interval. This subtraction scheme avoids the slow temperature response of the model surface. The principle of DIT has been confirmed with a thermal simulation [17] and the method works reliably for measuring unsteady boundary

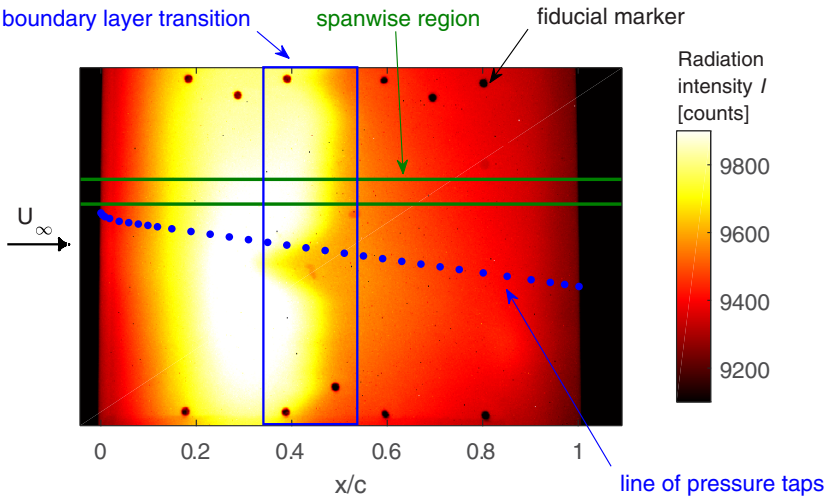

Figure 3. Infrared image of the airfoil model suction surface.

layer transition on different setups, from pitching airfoils to large scale rotor test rigs [24, 25]. A variant of the DIT method has been used to observe static and dynamic stall [26, 27]. Wolf *et al* [18] recently performed an optimization of the DIT method for unsteady transition detection on a pitching airfoil model, based on the recommendations given in [17]. An example result of this study is shown in figure 1 in comparison to reference measurements from the σC_p-technique. The figure shows the detected transition positions x_{tr}/c versus angle of attack α on the upper side of a pitching airfoil, also revealing hysteresis effects. Two distinct differences between the DIT result and the reference data remain after the optimization of DIT, a considerable phase difference during the pitching motion upstroke and the inability to resolve the downstream turning point of the transition movement with DIT due to the decreased radiation signal in that region.

3. Setup

The experimental setup for this study is identical to that described in [18], to which the reader is referred for a more detailed description of the hardware components, experimental layout and data processing procedures. A DSA-9A helicopter airfoil model made out of carbon fiber-reinforced epoxy (chord length $c = 0.3$ m, span width $s = 0.997$ m) is measured in the open jet '1MG' wind tunnel of DLR Göttingen at $V_\infty = 50$ m s^{-1} ($Ma = 0.14$, $Re = 1 \times 10^6$). The model pitches around its quarter-chord axis, driven by an electric actuation mechanism. This study examines data for test cases with pitch angle $\alpha(t) = 4° - \alpha_1 \cos(2\pi f \times t)$, where $\alpha_1 = 6°$ and $f = 2$ Hz (reduced frequency $k = (\pi f \times c)/V_\infty = 0.038$) or $f = 4$ Hz (reduced frequency $k = 0.075$). The airfoil model is equipped with Kulite fast-response pressure sensors installed under the model surface that are sampled at 200 kHz. The boundary layer transition location is determined from the pressure sensor signals using the σC_p-technique. The test time is 50 s, during which 5000 infrared images with a Flir SC7750-L camera (511 × 636 pixels, noise-equivalent temperature difference 35 mK) of the model suction surface are taken using an integration time of 0.19 ms. The image acquisition frequency is 99.98 Hz, slightly detuned from the pitching motion frequency, which allows the resolution of the period with 5000 points from multiple pitching motion cycles in $\Delta(f \times t) = 2 \times 10^{-4}$ increments. The airfoil model is externally heated with a 1.5 kW spotlight to establish a temperature difference between the model and the flow of approximately $\Delta T \approx 12$ K. The experimental setup is sketched in figure 2.

A sample infrared image from this setup, taken at a static angle of attack $\alpha = 1.5°$ is given in figure 3. In this single measurement with $k = 0$, the boundary layer transition region can be identified at $x/c \approx 0.45$ from the spatial radiation intensity gradient, however, Wolf *et al* illustrate in [18] how this method fails for $k > 0$. A turbulent wedge is present in the model center, where the boundary layer transition location is visibly moved upstream. The turbulent wedge persists at the same spanwise location in all measurements and its occurrence is therefore accredited to the locally increased surface roughness resulting from a small model surface defect. For the further analysis of the thermographic data, the measured radiation intensities per pixel are mapped to the chord length and averaged over the spanwise region indicated in green in figure 3. A fully converged periodic surface temperature behavior could not be achieved in the experiment, the long-term temperature drift is corrected as described in [18]. Since the employed data analysis methods do not rely on absolute temperature levels, a conversion of the measured radiation intensity I to temperature T is not performed in this study and the infrared camera measurements are given in counts.

The simulation results analyzed in this study are produced with a coupled simulation of the unsteady aerodynamics of a pitching DSA-9A airfoil with the 2D URANS code DLR-TAU and of the airfoil suction surface temperature with a thermal FEM model. The simulations are loosely coupled, which means that the CFD solution is computed first and the results are used as input to the thermal FEM model. The simulations have been set up and performed by Gardner *et al*, as described and reported in [17]. The flow conditions for the CFD simulation

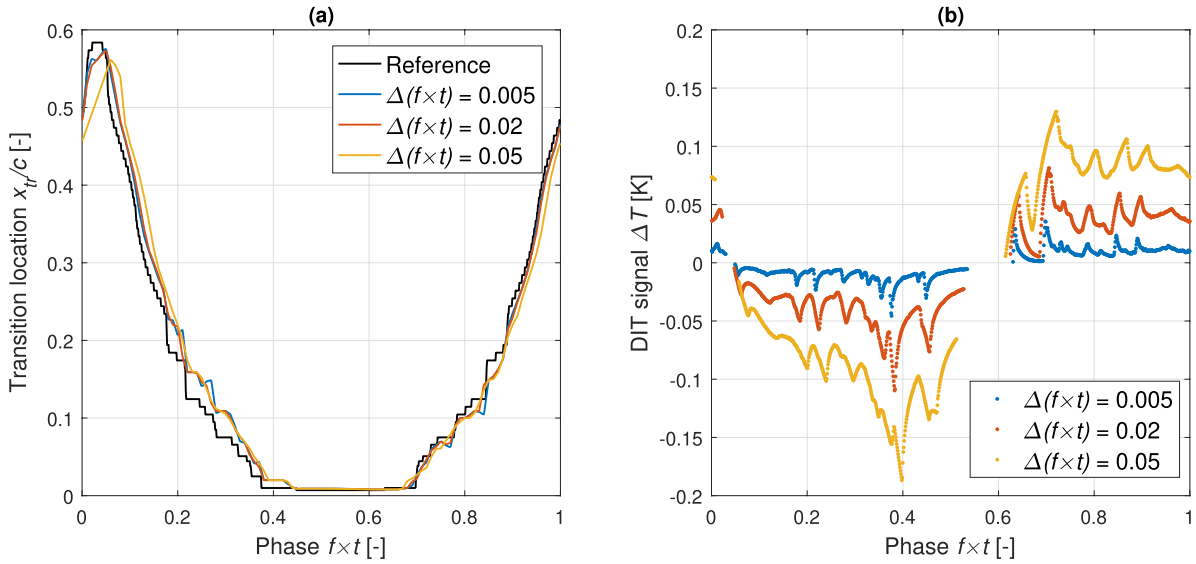

Figure 4. Effects of varying $\Delta(f \times t)$ when performing DIT on the simulation data: (a) effect on the DIT transition location, (b) effect on the DIT signal.

are $Ma = 0.30$ and $Re = 1.8 \times 10^6$. The pitching motion is described by $\alpha(t) = 4.3° - 6° \cos(2\pi f \times t)$ with $f = 6.6$ Hz (reduced frequency $k = 0.060$). The unsteady boundary layer transition is modeled with an external boundary layer procedure based on the e^N-method with an amplification factor of $N = 10$, and then fed back to the flow solver for each time step. The skin friction distributions $C_f(x,t)$ and pressure distributions $C_p(x,t)$ are saved as results from the URANS simulation. The reference unsteady transition location is determined from the skin friction result, it corresponds to the location of the maximum gradient $(\partial C_f/\partial x)_{\max}$.

For the thermal FEM model, the skin friction results are used to calculate the heat transfer by means of the Reynolds analogy. In this thermal model, only the wall normal conduction is modeled. The airfoil surface is modeled as uniform material with the thermal properties of epoxy. To represent the incoming heat flux from the spotlight H_L in the model, a constant heat source is imposed at the top element in the thermal model. The parameters for the thermal FEM simulation are summarized in table 1. The result of the simulation is the unsteady surface temperature distribution over the pitching motion period $T(x,t)$.

Table 1. Thermal FEM simulation parameters [17].

Parameter	Value
Cells in vertical direction	800
Wall thickness	5.5 mm
Simulation time step	5×10^{-5} s
Thermal conductivity κ	0.5 W (m × K)$^{-1}$
Heat capacity C_P	2300 J (kg × K)$^{-1}$
Material density ρ	1180 kg m^{-3}
Lamp heat flux H_L	2000 W m^{-2}

4. Effect of varying the DIT image separation time step

In order to design an automated optimization procedure for the DIT image separation time step, a detailed understanding of its effect is required. The previous studies suggest that relatively large DIT time steps introduce systematic measurement errors, while smaller time steps produce also smaller temperature differences. In the following, DIT is applied to the results of the unsteady surface temperature computation from the simulation. The DIT transition measurement, at a given phase in the oscillation cycle, is the location of the maximum absolute temperature difference between two subtracted temperature distributions. The DIT signal is the value of this temperature difference. The results for the DIT transition measurement and the DIT signal over the pitching motion period are shown for three different DIT image separation time steps $\Delta(f \times t)$ in figure 4. The transition location from the analysis of C_f is shown for reference.

The DIT measurement phase lag with respect to the reference increases with increasing $\Delta(f \times t)$, and the DIT signal increases with increasing $\Delta(f \times t)$, as further discussed in [17]. Note that the spikes in the DIT signal have no physical meaning, they result from a discrete propagation of the transition location in the simulation. The non-smooth transition movement also produces some scatter in the DIT transition measurements, in particular for the smaller $\Delta(f \times t)$. A part of the motion period cannot be measured with DIT because the regions with forward and backward moving transition were separated to avoid systematic measurement errors. Boundary layer transition does not occur downstream of $x/c > 0.6$ in this configuration, therefore all DIT data points where $x_{tr}/c > 0.6$ have been removed from the result. These outliers occur when the boundary layer transition position remains unchanged during the DIT time step. Remaining outliers in the DIT transition measurement are removed with a median filter of window size 5, in the last step the filtered values for x_{tr}/c are linearly interpolated.

In figure 5, the DIT measurement error, averaged over the motion period, is shown versus $\Delta(f \times t)$. The transition

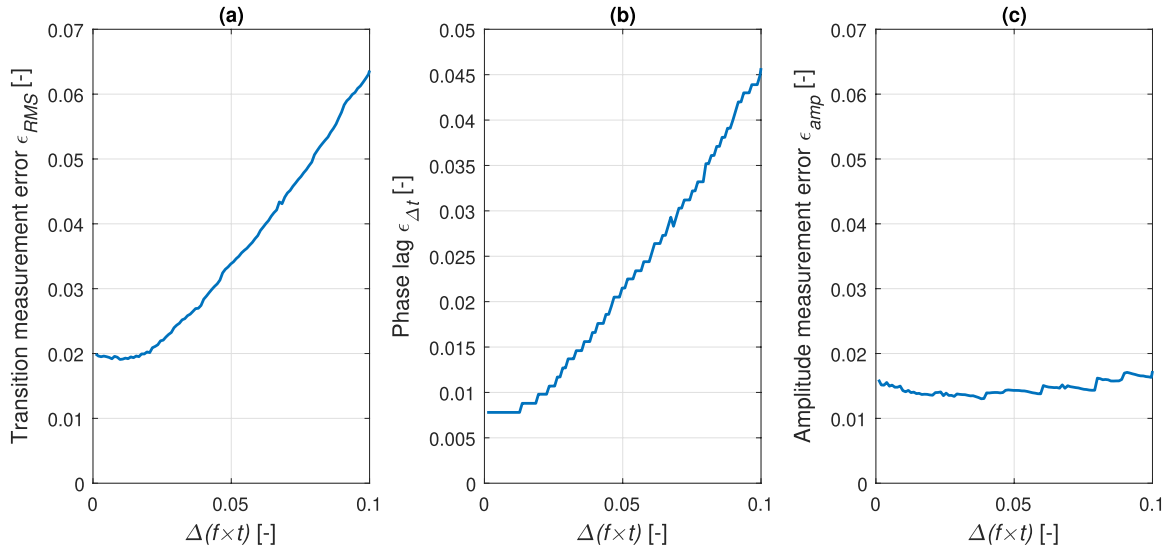

Figure 5. DIT transition measurement error over $\Delta(f \times t)$: (a) total measurement error, (b) phase lag, (c) amplitude measurement error.

measurement error ϵ_{RMS} is defined as a root-mean-square of the difference between the DIT result and the reference transition. The total error is split into two components, the phase lag error $\epsilon_{\Delta t}$ and the amplitude measurement error ϵ_{amp}. The phase lag error is determined with a cross-correlation of the DIT transition measurement and the reference transition. The number of samples corresponding to the cross-correlation peak is converted into the phase lag error $\epsilon_{\Delta t}$. The amplitude measurement error is the remaining root-mean-square error after the phase lag error is corrected by shifting the DIT transition in phase by $\epsilon_{\Delta t}$. It originates from the discretization of the problem in the simulation setup. The transition measurement error decreases nearly linearly from $\Delta(f \times t) = 0.1$ until $\Delta(f \times t) = 0.02$ and is approximately constant between $0 < \Delta(f \times t) < 0.02$. The value of ϵ_{amp} is not changing by more than ± 0.003. The phase lag error decreases with decreasing $\Delta(f \times t)$, this effect diminishes for the smallest $\Delta(f \times t)$ and a phase lag error of $\epsilon_{\Delta t} \approx 0.008$ remains. Thus, using $\Delta(f \times t) < 0.01$ reduces the phase lag well below 1% of the period, such that the amplitude measurement error remains as the major contribution to the total error.

5. Optimization of the DIT time step

5.1. Automated selection of the DIT time step

The findings of the analysis of the simulation results are used to develop a systematic optimization procedure for analyzing experimental data. This can be achieved by implementing an automated selection of the DIT time step. To perform this automated selection, the procedure consisting of the following steps is implemented.

- Perform DIT for all 5000 data points with each available DIT time step within $0 < \Delta(f \times t) < 0.1$, producing 4999 DIT measurements over the period for each individual $\Delta(f \times t)$.
- During the upstroke the transition location is expected to move upstream, during the downstroke it is expected to move downstream. The direction of the transition movement determines the sign of the measured DIT signal, which is therefore used to filter random outliers from the transition measurement.
- Filter outliers from the DIT measurements with a sanity check of the measured transition location based on static polar data. The unsteady transition location for an instantaneous $\alpha(t)$ is excepted within $\pm 0.25c$ of the transition location at the same α in steady flow conditions.
- Group the DIT measurements into 100 equally spaced time bins for each $\Delta(f \times t)$.
- Perform a discrete-continuous transformation of the DIT measurements in each bin for each $\Delta(f \times t)$ to a normalized probability density function.
- Save the peak P of the normalized probability density function as transition measurement result x_{tr}/c for the respective bin.
- The x_{tr}/c-result for a bin is filtered when the corresponding P is smaller than 10% of the median value of P over the period.
- For each $\Delta(f \times t)$, average the values of P for all bins to a 'certainty parameter' defined as $\overline{P}$.

The certainty parameter $\overline{P}$ that results from this procedure rises steeply from $\overline{P} = 0$ at $\Delta(f \times t) = 0$ to a nearly constant value at $\Delta(f \times t) \approx 0.03$, as shown for various experimental conditions in figure 6. For the optimization, a small DIT time step is desirable, hence $\Delta(f \times t)$ should be as small as possible while the result is still reliable, i.e. $\overline{P}$ is not too low. This requirement can be implemented by selecting a threshold for $\overline{P}$ and using the first $\Delta(f \times t)$ that exceeds this threshold as the optimum. For this study, the threshold $0.8 \times \overline{P}_{\mathrm{max}}$ is selected, where $\overline{P}_{\mathrm{max}}$ is the maximum of $\overline{P}$ for each respective test case over all $\Delta(f \times t)$. The DIT transition measurement result with the smallest $\Delta(f \times t)$ where $\overline{P}$ is larger than the

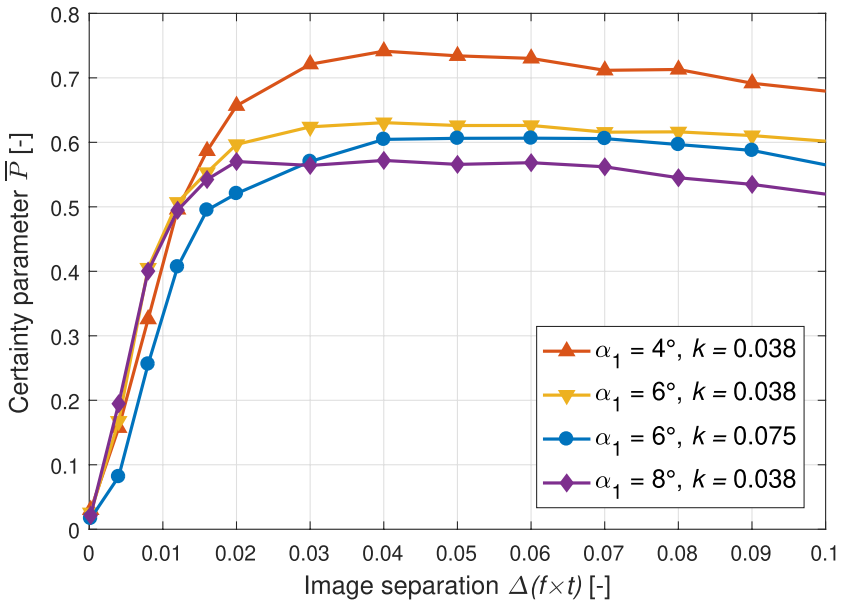

Figure 6. Certainty parameter $\overline{P}$ over $\Delta(f \times t)$ in the experiment.

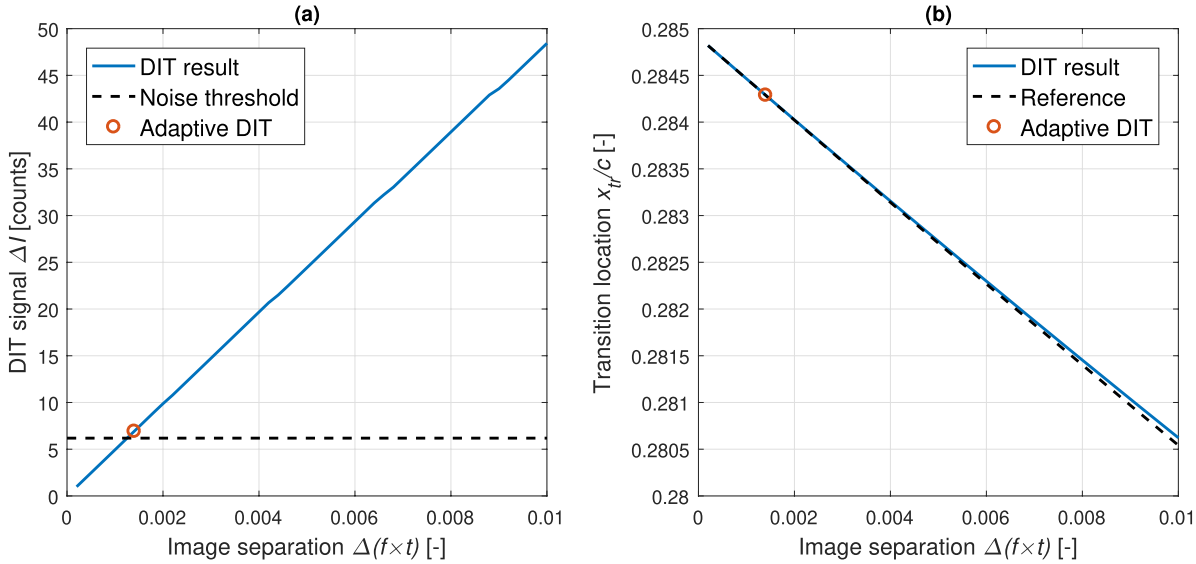

Figure 7. Schematic of the working principle of ADIT for a fixed first image: (a) DIT signal over $\Delta(f \times t)$, (b) DIT measurement and true reference transition.

threshold (typically $0.01 < \Delta(f \times t) < 0.02$) will be referred to as optimized DIT result in the following.

5.2. Adaptive time step DIT (ADIT)

A different approach to optimizing the DIT method is adaptive time step DIT (ADIT), where the image separation time step between the two subtracted IRT measurements is not constant over the motion period, but automatically adapted according to a specified criterion for the measured DIT signal. The idea behind this application is that the ADIT method provides a transition measurement with a smaller measurement error compared to conventional DIT, particularly for thermographic measurements with varying signal strength. The working principle of ADIT is illustrated schematically in figure 7, based on synthetic data resembling the experiment. The criterion for the automated selection of the DIT time step is based on the DIT signal ΔI and a noise threshold level t_n. In figure 7(a), ΔI as it depends on the time step is shown together with the noise threshold t_n. If $\Delta(f \times t)$ is too small, ΔI is below the threshold t_n and no valid DIT transition measurement result can be obtained when using real data. The ADIT algorithm automatically selects the first $\Delta(f \times t)$ that produces a sufficient DIT signal $\Delta I > t_n$. This reduces the DIT transition measurement error as far as possible within the limits of the available signal, as illustrated in figure 7(b).

In the following, the ADIT method is implemented for the experimental test case with $k = 0.038$. The noise threshold t_n for the application of ADIT is specified as the minimum absolute value of the DIT signal over the entire period for the

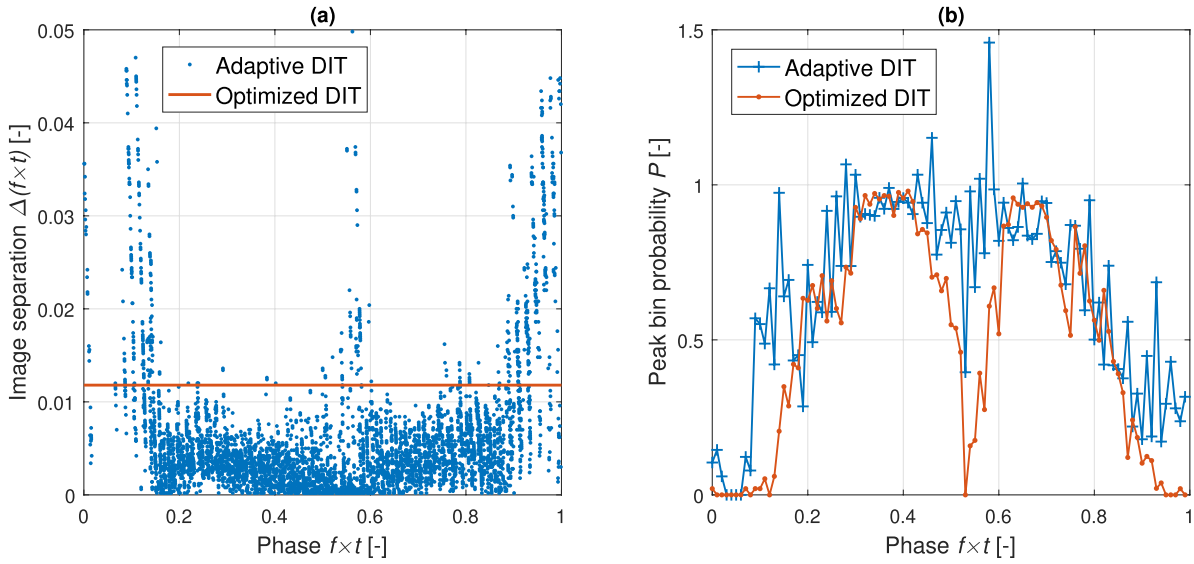

Figure 8. Application of ADIT to the experimental data: (a) adapted and optimized constant $\Delta(f \times t)$, (b) peak probability per time bin with ADIT and optimized DIT.

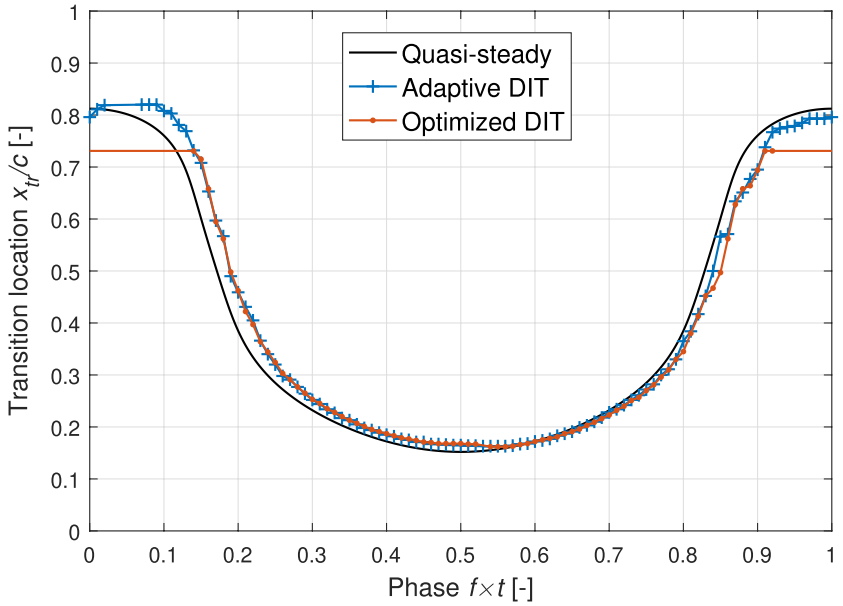

Figure 9. Transition measurement with ADIT and optimized DIT.

respective $\Delta(f \times t)$, with an additional margin of five camera counts, which is sufficient to remove random outliers, hence $t_n(\Delta(f \times t)) = \Delta I_{\text{noise}}(\Delta(f \times t)) + 5$. As an additional constraint, the maximum allowed $\Delta(f \times t)$ is 0.1. The implementation of ADIT is illustrated in figure 8. The working principle of ADIT is shown by the adapted $\Delta(f \times t)$ in comparison to the optimized constant $\Delta(f \times t)$. For the largest part of the period, the adapted time step is smaller than the optimized constant $\Delta(f \times t)$. When the transition movement slows down near the motion turning points, the DIT signal strength ΔI decreases and the adapted time step $\Delta(f \times t)$ increases accordingly. The functioning of the ADIT approach is demonstrated by the values of P for each time bin in the post-processing procedure of ADIT and optimized DIT. It can be deduced from the comparison of P over phase that the ADIT method produces more valid transition measurement data points over the period, i.e. more data points that are not filtered with the post-processing algorithm and thus $\overline{P}_{ADIT} > \overline{P}_{DIT}$. Several ADIT data points accumulate when the transition movement speed is changing and $\Delta(f \times t)$ is adapted accordingly, causing a local increase of $P > 1$ as peaks of the normalized probability density function there.

Figure 9 shows the transition location result obtained with ADIT using the same transition measurement data post-processing procedure as for optimized DIT, which is shown for comparison. For reference, the quasi-steady transition prediction is shown as well. The transition measurement results from ADIT and optimized DIT are essentially identical for $0.15 < f \times t < 0.9$. However, ADIT is able to measure the transition movement also around the downstream turning point, while optimized DIT produces no valid data in this region. Considering the agreement with the behavior of the

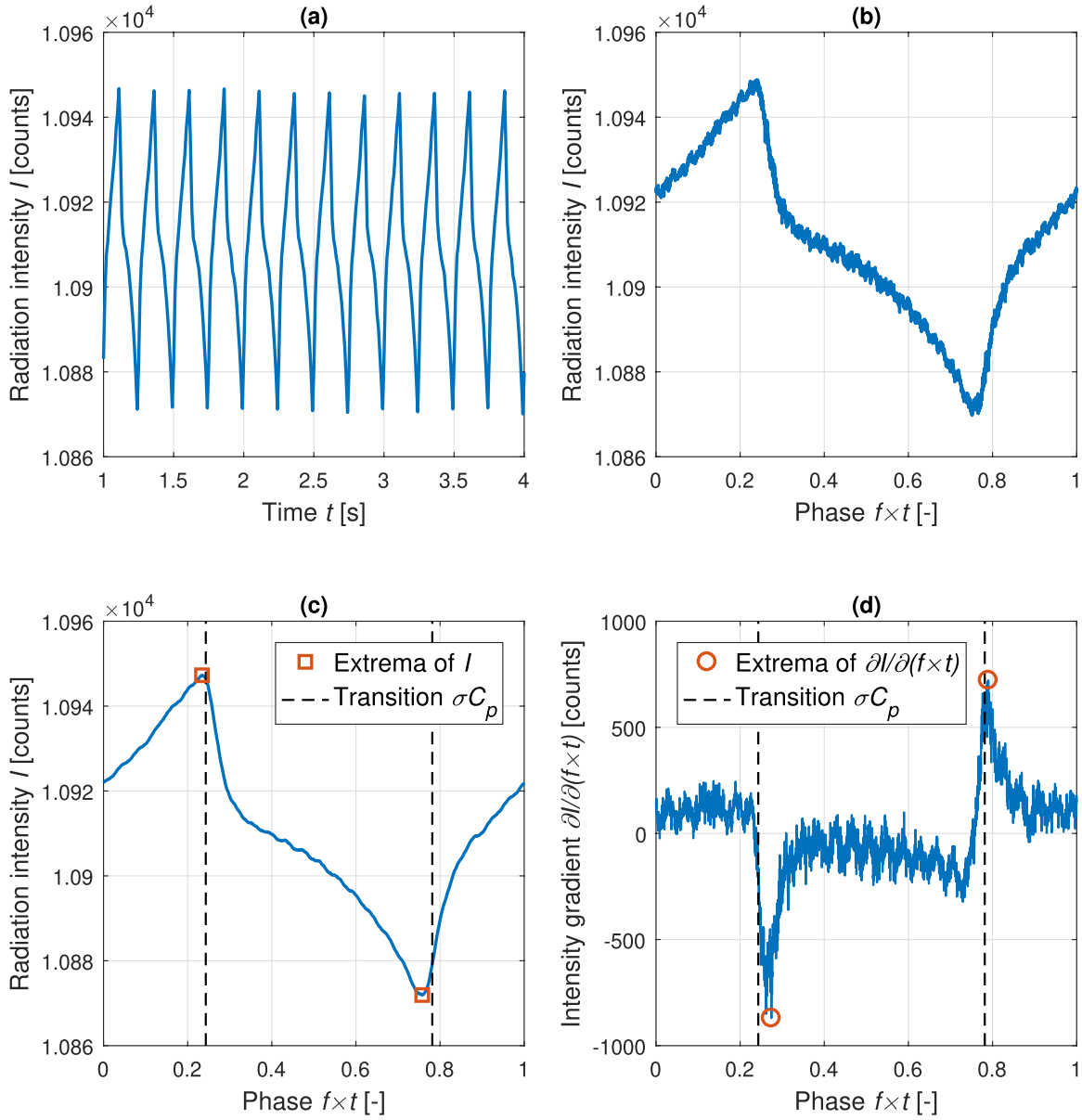

Figure 10. LIT signal processing steps at $x/c = 0.31$: (a) intensity signal over time, (b) signal ordered in phase, (c) smoothed intensity signal, (d) intensity gradient.

quasi-steady transition at the downstream turning point, the transition measurement results from ADIT in this region appear correct.

6. Local infrared thermography (LIT)

6.1. Principle and application

An alternative data analysis method for the IRT measurements is local infrared thermography (LIT), which is based on evaluating the time variation of the surface temperature (or radiation intensity I) signal at fixed locations on the model surface. The data processing procedure for the application of LIT to the experimental test case with $k = 0.075$ is illustrated in figure 10 for the chord position $x/c = 0.31$. This chord position is selected because a pressure sensor is installed there on a different spanwise position, so that reference transition phase instants determined with σC_p are available.

The radiation intensity signal over time $I(t)$ shown in figure 10(a) is ordered in phase in accordance with the simultaneously measured $\alpha(t)$, see figure 10(b). Because the ordered signal is too noisy for an accurate direct computation of the finite difference gradient, a moving-average smoothing (window size $\pm 1\%$ of the period) is performed, resulting in the curve shown in figure 10(c). Then, the intensity gradient $\partial I/\partial(f \times t)$ was computed from finite differences, see figure 10(d). Figures 10(c) and (d) mark the extrema of the shown signals and also show the boundary layer transition instants in phase as determined with the σC_p-analysis of the pressure signal.

For this chord position $x/c = 0.31$, the boundary layer flow in the center of the period ($0.24 < f \times t < 0.78$) is turbulent,

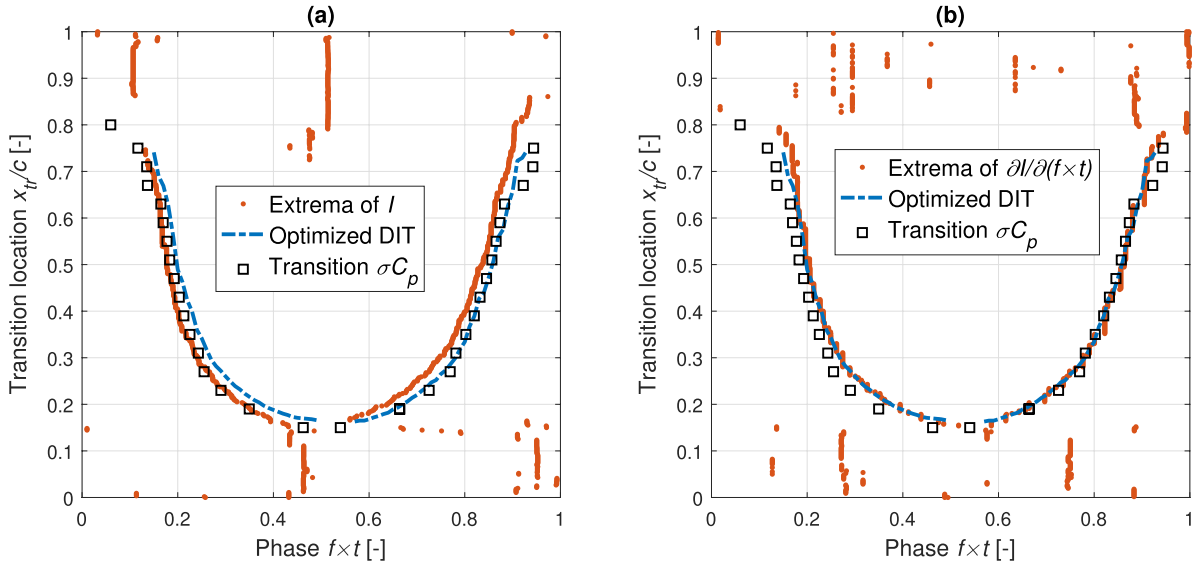

Figure 11. Results before post-processing from the analysis of (a) I and (b) $\partial I/\partial(f \times t)$, with σC_p-measurements for reference.

and at the beginning and end of the period the flow is laminar. The intensity signal in figure 10(c) is generally increasing when the experienced flow is laminar and decreasing when turbulent. This can be explained with the different heat transfer levels corresponding to either a laminar or turbulent boundary layer and the slow temperature response of the airfoil model surface compared to the pitching motion period. The extrema of the intensity curve are therefore connected to the boundary layer transition passing this location. The reference transition measured with σC_p confirms this. It is noted that the detected peaks are leading the reference transition in phase by -0.91% of the period on the motion upstroke (local boundary layer transition to turbulence) and by -2.39% of the period on the motion downstroke (local relaminarization).

The analysis of the local intensity gradient in figure 10(d) reveals two distinct peaks that correlate with the occurrence of boundary layer transition as well. These peaks appear shortly after the intensity signal has reached its extremum and after the σC_p transition location, the phase lag is 3.12% of the period during the pitching motion upstroke and 0.85% of the period on the downstroke. The physical argument for relating these peaks to boundary layer transition is that the laminar boundary layer causes surface warming and the turbulent boundary layer causes surface cooling when no thermal equilibrium is reached.

In figure 11, the described LIT approach is applied to all sampled chord locations. It shows the individual results for the extrema of I (figure 11(a)) and $\partial I/\partial(f \times t)$ (figure 11(b)) as dots in comparison to the boundary layer transition location measurements with optimized DIT and σC_p. In general, the observations from the analysis of $x/c = 0.31$ can be extended to the entire chord length. However, peaks in the signal are also detected when no boundary layer transition occurs at the respective location according to the DIT and σC_p measurements (in figure 11 upstream of $x/c \approx 0.15$ and downstream of $x/c \approx 0.8$). At these locations, the local temperature signal shows a peak-and-trough behavior which is not associated with the occurrence of boundary layer transition. Instead, it is linked to the periodic pitching motion and the resulting periodic changes in the flow field around the airfoil. This leads to the occurrence of the temperature extrema around the extrema of the pitching motion, hence around $f \times t = 0.5$ and near $f \times t = 0$ or $f \times t = 1$ in figure 11(a).

The data processing of the measured extrema follows three steps. First, the analysis of the data points is restricted to regions where boundary layer transition is expected to occur based on static polar data. This is achieved by evaluating the static transition polar at the smallest and largest α of the pitching motion, adding a margin of $0.1c$ and removing data points that appear outside of the region in between. In the next step, the transition points x_{tr}/c are extracted for each point in phase using 100 equally spaced time bins over the period and taking the median x/c value of the data points in each bin. Finally, the resulting transition movement over phase is smoothed using a median filter with kernel size 3.

There is no qualitative difference between the results from the LIT intensity gradient analysis and optimized DIT in figure 11(b). Since both transition measurement methods are based on the same physical argument, it is noted here that performing DIT with a small $\Delta(f \times t)$ and detecting the peaks of the local intensity gradient are equivalent operations. Filtered LIT results from the analysis of the extrema of I are compared to DIT and σC_p results in detail in the following chapter.

6.2. Application to two-dimensional IRT data

The LIT approach can be readily extended from the shown one-dimensional analysis to analyzing the entire airfoil model surface. For that, the image data processing procedure is adjusted from the analysis of spanwise averaged data to single pixels. The individual results per pixel from the LIT method are connected to a boundary layer transition front by marking each pixel as 'transitional' for the determined extremum phase instant over $\pm 1\%$ of the period and then computing the

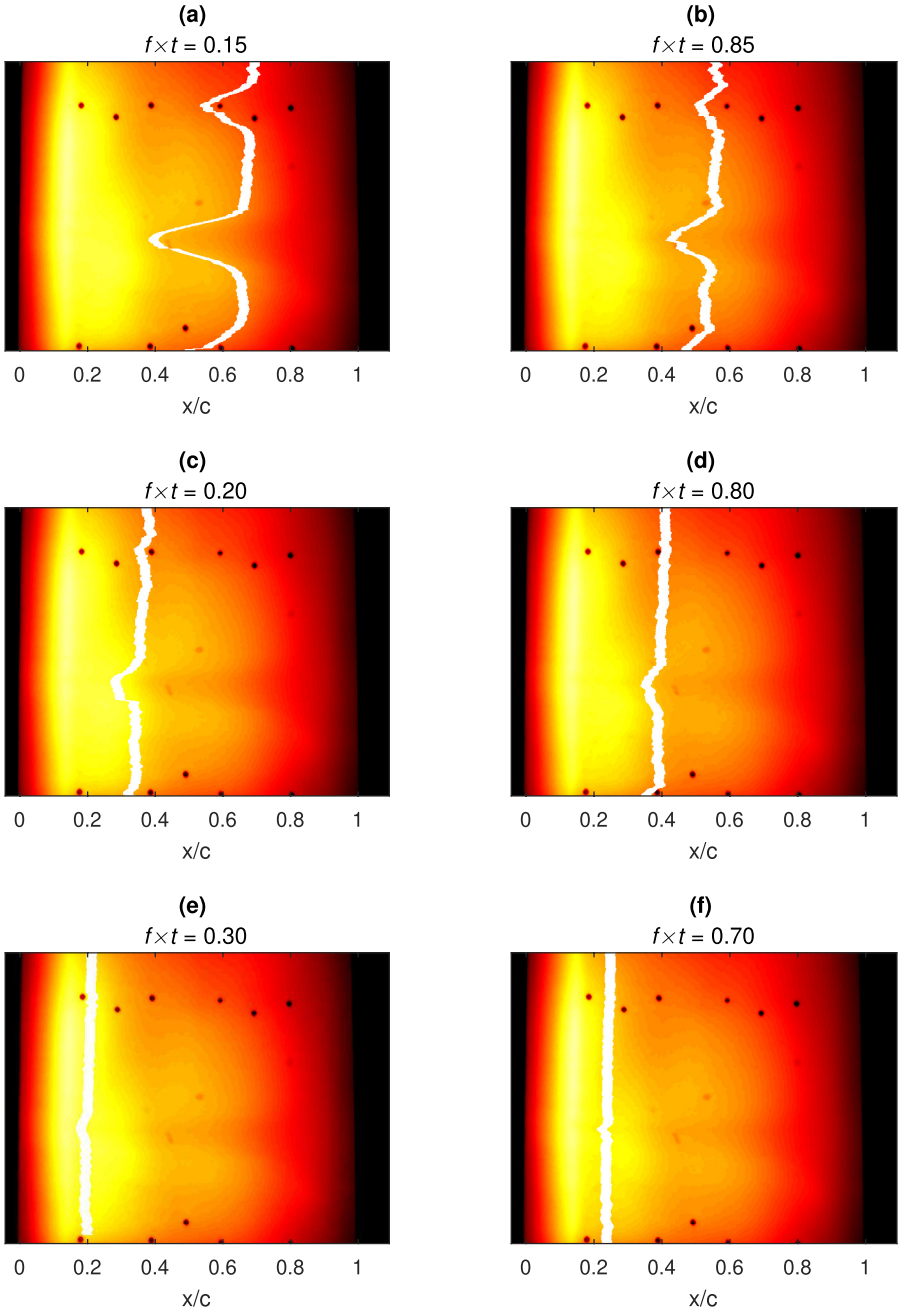

Figure 12. LIT measurements of the two-dimensional transition front.

median location of the transitional pixels for each streamwise pixel array.

Figure 12 shows the boundary layer transition front determined with LIT for three phase instants on the upstroke (figures 12(a), (c) and (e)) and downstroke (figures 12(b), (d) and (f)). Flow is from left to right, darker regions are colder and the boundary layer transition front is shown in white. The six example phase instants are selected such that images shown side by side are from the same instantaneous angle of attack $\alpha(t)$. Note that the plotted positions of the transition fronts determined with LIT cannot be deduced directly from the individual thermographic images in the background of figure 12 due to the slow temperature response of the surface material compared to the pitching motion frequency.

The measured boundary layer transition fronts reveal that transition is triggered early in the model center and on the sides. In particular, the turbulent wedge in the model center is more pronounced during the upstroke and when the transition front is further downstream. As a quantification of this premature transition, the transition measurement difference between the spanwise region that was used for the one-dimensional analysis and the most upstream transition point is $\Delta x/c \approx 0.15$ during the upstroke at $f \times t = 0.15$ and $\Delta x/c \approx 0.09$ during the downstroke at $f \times t = 0.85$. It is noted that neither of these features of the boundary layer transition front, nor the visible surface defects on the airfoil model decrease the effectiveness of the LIT technique.

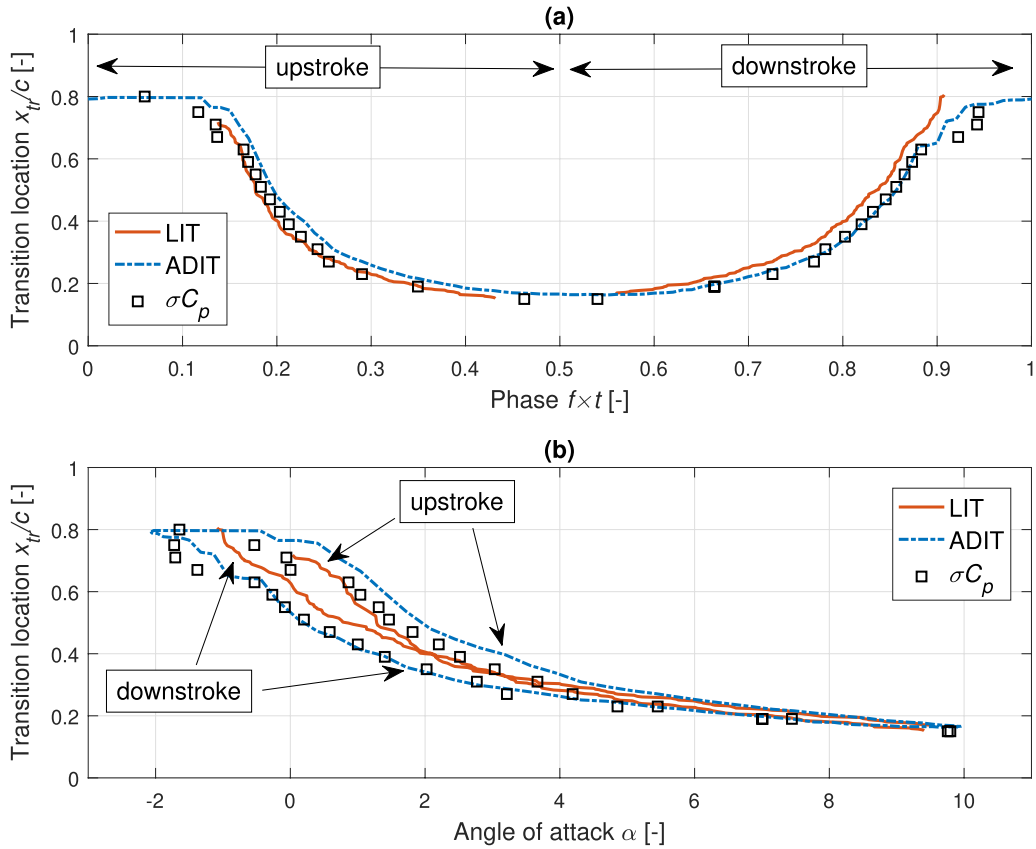

Figure 13. Transition measurements with LIT, DIT and σC_p.

The pixelwise LIT results shown in figure 12 are based on the analysis of the extrema of the radiation intensity per pixel. The same procedure can be applied for the intensity gradient extrema, however the implementation without computing the gradient is computationally cheaper and produces a smoother behavior of the boundary layer transition over phase with the described post-processing activities.

7. Comparison of the methods

In figure 13, the transition measurement results for $k = 0.075$ from the LIT intensity peak detection and ADIT are shown together with the reference transition measurements from the fast-response σC_p-technique. The figure includes two graphical representations of the same measurement results; while the transition location plotted over phase (figure 13(a)) is useful to investigate the transition location during the upstroke and the downstroke separately, the hysteresis plot over angle of attack α (figure 13(b)) is particularly useful to investigate the unsteady aerodynamics effects on the transition measurement results.

The following observations are made.

- The transition measurements from LIT and ADIT are in good qualitative agreement during the upstroke and the downstroke. ADIT measures the entire transition motion over the period while LIT is not, as it fails to return reliable results for the downstream transition point reversal. The LIT measurements lead the ADIT measurements in phase by up to 5% of the period and the measurements from LIT and ADIT show qualitative differences near the motion turning points.
- The σC_p-measurements downstream of $x/c = 0.65$ show a step compared to the measurements further upstream. This step produces transition measurements further upstream than expected from a smooth curve during the beginning and end of the motion period.
- The comparison of the results from LIT and σC_p suggests that the LIT results near the motion turning points do not capture the onset of the transition motion in the changed direction. Instead, LIT measures spurious transition locations after the motion has stopped on the motion downstroke.
- The LIT measurements lead the σC_p transition in phase during the downstroke by up to 5% of the period, during the upstroke this phase difference is systematically reduced to less than 3% of the period.
- The results from ADIT and σC_p are in very good qualitative and quantitative agreement. Both techniques reproduce the entire transition movement without exhibiting distinct overall systematic measurement errors and with a small level of random scatter in the data.
- The implementation of the data processing and analysis steps of LIT is simplified compared to DIT or ADIT and the computational effort is reduced.

While the measurements from ADIT and σC_p are in excellent agreement for the downstroke, a considerable difference

between ADIT and σC_p is observed during the upstroke. A systematic measurement phase lag of approximately 3% of the period is introduced, which results in a transition measurement difference of up to $\Delta x_{tr}/c \approx 0.07$ during mid-upstroke. An explanation for this difference is the variation in the dynamic behavior of the turbulent wedge in the model center during the up- and downstroke. The pressure taps for the σC_p measurements are located in the center of the airfoil model and are therefore affected by the turbulent wedge. With the two-dimensional implementation of LIT, it was found that the length of the turbulent wedge varies by $\Delta x/c \approx 0.06$ during the motion upstroke and downstroke. This means that the variation in the length of the turbulent wedge is at the order of magnitude of the transition measurement difference between ADIT and σC_p.

8. Conclusions

Advanced infrared thermography data processing methods for measuring unsteady boundary layer transition have been explored in this study. The analyzed data was measured on the suction surface of a pitching airfoil model in the wind tunnel with an infrared camera. The already established differential infrared thermography (DIT) method for measuring unsteady boundary layer transition has been automated and extended in this study. The newly introduced adaptive DIT approach with variable time separation produces more valid transition measurements over the period than optimized DIT with a constant time separation. The ADIT transition measurement result is in very good agreement with reference measurements from the σC_p-technique. Considerable systematic differences between the ADIT and σC_p results remain during the relaminarization on the pitching motion upstroke.

An alternative discussed measurement approach is local infrared thermography (LIT), where the measured radiation signal is analyzed at fixed locations. When analyzing the extrema of these signals, the produced result is an unsteady boundary layer transition measurement over phase comparable in accuracy to the result from optimized DIT. The argumentation for using the extrema as indicators for the occurrence of boundary layer transition is the different heat transfer behavior of laminar and turbulent boundary layers. It is observed in the temperature signal that the temperature decreases during the part of period where the boundary layer flow is turbulent and increases when the flow is laminar, which is expected from the difference in heat transfer (in view of the different skin friction levels and the Reynolds analogy) and from the slow temperature response of the airfoil model surface material relative to the pitching motion period.

As an alternative to analyzing the extrema of the signal, the temporal gradient of the measured signal can be analyzed as well. The local gradient shows two distinct peaks on the up- and downstroke, which can be extracted and interpolated to a boundary layer transition result that is equivalent to the result from optimized DIT with a constant time separation. The data processing activities are reduced with the LIT approach compared to DIT, because no optimization of the DIT image separation time step has to be performed and the post-processing of the results is simplified.

LIT can be extended to the investigation of the entire model surface by applying the measurement scheme at single pixel level. This approach allows the examination of the unsteady two-dimensional behavior for the boundary layer transition front in a level of detail that could not be achieved with any other technique before. A turbulent wedge is observed in the airfoil model center, where the pressure taps are located. The analysis of the dynamic behavior of the turbulent wedge provides a convincing explanation for the remaining differences between the ADIT and σC_p transition measurement results.

The LIT approach relies on a densely spaced sampling of the signal over time, which makes it useful only for periodic unsteady processes with the currently feasible sampling rates for infrared cameras and unsteady phenomena at technically relevant motion frequencies. The DIT method is not as limited in terms of flow conditions, it has been applied successfully to quasi-steady as well as highly unsteady flows in previous studies. However, in order to reduce the systematic DIT measurement error, the image separation time step has to be decreased until the DIT signal can be just identified in the random noise of the infrared camera. Therefore, sophisticated DIT transition measurement outlier removal strategies are needed, as those presented in this study.

In future studies, the unsteady boundary layer transition detection methods presented in this study can be applied to any three-dimensional wing geometry in unsteady periodic wind tunnel experiments. As the methods are based on the optical IRT technique, they can be applied to all model scales and no instrumentation of the model is required. This makes the methods particularly useful for rotating systems, from model rotors in the laboratory to full scale flight testing on helicopter rotors.

Acknowledgments

The studies were conducted in the framework of the DLR project ‘FAST-Rescue’.

ORCID iDs

C Mertens https://orcid.org/0000-0002-3210-6219
C C Wolf https://orcid.org/0000-0002-9052-7548
A D Gardner https://orcid.org/0000-0002-1176-3447
F F J Schrijer https://orcid.org/0000-0002-7532-4320
B W van Oudheusden https://orcid.org/0000-0002-7255-0867

References

[1] Heister C C 2018 A method for approximate prediction of laminar-turbulent transition on helicopter rotors *J. Am. Helicopter Soc.* **63** 1–14
[2] Monson D J, Mateer G G and Menter F R 1993 Boundary-layer transition and global skin friction measurement with

an oil-fringe imaging technique *Soc. Automot. Eng. SAE Tech. Pap.* 932550
[3] Aeschliman D P, Croll R H and Kuntz D W 1995 Shear-stress-sensitive liquid-crystals for hypersonic boundary-layer-transition detection *J. Spacecr. Rockets* **32** 749–57
[4] Asai K, Kanda H, Kunimasu T, Liu T S and Sullivan J P 1997 Boundary-layer transition detection in a cryogenic wind tunnel using luminescent paint *J. Aircr.* **34** 34–42
[5] Lorber P F and Carta F O 1992 Unsteady transition measurements on a pitching three-dimensional wing *NASA Report* NASA-CR-193000 N93–27450 (https://ntrs.nasa.gov/search.jsp?R=19930018261)
[6] Schreck S J, Faller W E and Helin H E 1998 Pitch rate and Reynolds number effects on unsteady boundary-layer transition and separation *J. Aircr.* **35** 46–52
[7] Lee T and Basu S 1998 Measurement of unsteady boundary layer developed on an oscillating airfoil using multiple hot-film sensors *Exp. Fluids* **25** 108–17
[8] Goerttler A, Gardner A D and Richter K 2018 Unsteady boundary layer transition detection by automated analysis of hot film data *New Results in Numerical and Experimental Fluid Mechanics XI* (*Notes on Numerical Fluid Mechanics and Multidisciplinary Design* vol 136) ed A Dillmann *et al* (Cham: Springer)
[9] Gardner A D and Richter K 2015 Boundary layer transition determination for periodic and static flows using phase-averaged pressure data *Exp. Fluids* **56** 119
[10] Richter K, Wolf C C, Gardner A D and Merz C B 2016 Detection of unsteady boundary layer transition using three experimental methods *54th AIAA Aerospace Sciences Meeting (San Diego, CA, USA)* (AIAA) 2016-1072 (https://doi.org/10.2514/6.2016-1072)
[11] Thomann H and Frisk B 1967 Measurement of heat transfer with an infrared camera *Int. J. Heat Mass Transf* **11** 819–26
[12] Bynum D S, Hube F K, Key C M and Dyer P M 1976 Measurement and mapping of aerodynamic heating in VKF tunnel B with an infrared camera *Arnold Engineering Development Center AEDC Technical Report* TR-76-54 (https://apps.dtic.mil/docs/citations/ADA033116)
[13] Stallings D W and Carver D B 1978 Infrared and phase-change paint measurements of heat-transfer on the space shuttle orbiter *Arnold Engineering Development Center AEDC Technical Report* TSR-78-V13 (https://apps.dtic.mil/docs/citations/ADA059796)
[14] Gartenberg E and Roberts A S 1992 Twenty-five years of aerodynamic research with infrared imaging *J. Aircr.* **29** 161–71
[15] Carlomagno G M and de Luca L 2001 Infrared thermography in convective heat transfer *Handbook of Flow Visualization* ed W J Yang (London: Taylor and Francis)
[16] Carlomagno G M and Cardone G 2010 Infrared thermography for convective heat transfer measurements *Exp. Fluids* **49** 1187–218
[17] Gardner A D, Eder C, Wolf C C and Raffel M 2017 Analysis of differential infrared thermography for boundary layer transition detection *Exp. Fluids* **58** 122
[18] Wolf C C, Mertens C, Gardner A D, Dollinger C and Fischer A 2019 Optimization of differential infrared thermography for unsteady boundary layer transition measurement *Exp. Fluids* **60** 19
[19] Astarita T and Carlomagno G M 2012 *Infrared Thermography for Thermo-Fluid-Dynamics* (*Experimental Fluid Mechanics*) ed W Merzkirch *et al* (Berlin: Springer) pp 5–21
[20] Schlichting H and Gersten K 2016 *Boundary-Layer Theory* (Berlin: Springer) pp 28–37
[21] Incropera F P, De Witt D P, Bergman T L and Lavine A S 2007 *Fundamentals of Heat and Mass Transfer* (Hoboken, NJ: Wiley) pp 384–5
[22] Simon B, Filius A, Tropea C and Grundmann S 2016 IR thermography for dynamic detection of laminar-turbulent transition *Exp. Fluids* **57** 93
[23] Raffel M and Merz C B 2014 Differential infrared thermography for unsteady boundary-layer transition measurements *AIAA J.* **52** 2090–3
[24] Raffel M, Merz C B, Schwermer T and Richter K 2015 Differential infrared thermography for boundary layer transition detection on pitching rotor blade models *Exp. Fluids* **56** 30
[25] Overmeyer A, Heineck J T and Wolf C C 2018 Unsteady boundary layer transition measurements on a rotor in forward flight *74th Annual Forum of the American Helicopter Society (Phoenix, AZ, USA)* 74-2018-0207 (https://vtol.org/store/product/unsteady-boundary-layer-transition-measurements-on-a-rotor-in-forward-flight-12692.cfm)
[26] Gardner A D, Wolf C C and Raffel M 2016 A new method of dynamic and static stall detection using infrared thermography *Exp. Fluids* **57** 149
[27] Raffel M, Gardner A D, Schwermer T, Merz C B, Weiss A, Braukmann J and Wolf C C 2017 Rotating blade stall maps measured by differential infrared thermography *AIAA J.* **55** 1753–6